frontiers in Remote Sensing

TYPE Original Research
PUBLISHED 29 May 2026
DOI 10.3389/frsen.2026.1742193

Check for updates

OPEN ACCESS

EDITED BY
K. R. Renjith,
Centre for Water Resources Development and Management, India

REVIEWED BY
Lixin Li,
Heilongjiang University of Science and Technology, China
Chang Fan,
China Agricultural University, China

*CORRESPONDENCE
Yu Wu,
wu_yu@tju.edu.cn

RECEIVED 08 November 2025
REVISED 05 March 2026
ACCEPTED 17 April 2026
PUBLISHED 29 May 2026

CITATION
Guo Y, Wu Y, Zheng L, Wang W, Chen Q, Han X, Xu C, Li P, Sun X, Zuo X, Ji M, Liu Z, Wu Y and Zhang X (2026) Assessing carbon storage of a coastal wetland using long-term high-resolution Gaofen satellite data.
Front. Remote Sens. 7:1742193.
doi: 10.3389/frsen.2026.1742193

COPYRIGHT
© 2026 Guo, Wu, Zheng, Wang, Chen, Han, Xu, Li, Sun, Zuo, Ji, Liu, Wu and Zhang. This is an open-access article distributed under the terms of the Creative Commons Attribution License (CC BY). The use, distribution or reproduction in other forums is permitted, provided the original author(s) and the copyright owner(s) are credited and that the original publication in this journal is cited, in accordance with accepted academic practice. No use, distribution or reproduction is permitted which does not comply with these terms.

Assessing carbon storage of a coastal wetland using long-term high-resolution Gaofen satellite data

Yanming Guo[1], Yu Wu[2]*, Lijuan Zheng[3], Wen Wang[1], Qian Chen[4], XingXing Han[2], Chongbin Xu[4], Pan Li[2], Xiaomin Sun[4], Xin Zuo[4], Mingyi Ji[2], Zhenxuan Liu[2], Yuhan Wu[2] and Xiyue Zhang[2]

[1]School of Ecology and Environment, Renmin University of China, Beijing, China, [2]Institute of Surface-Earth System Science, School of Earth System Science, Tianjin University, Tianjin, China, [3]Land Satellite Remote Sensing Application Center, Ministry of Natural Resources of China, Beijing, China, [4]Department of Satellite Application Technology, Beijing Institute of Space Mechanics and Electricity, Beijing, China

Wetland carbon sink is considered to be one of the most important components of the global carbon cycle. Space-borne remote sensing serves as a vital data source for the classification and carbon sink estimation of wetland. However, inadequate spatial resolution often impedes the accurate classification of different vegetation types, substantially affecting the precision of carbon sink assessments. We propose a framework for the accurate classification and dynamic carbon storage monitoring in coastal wetland vegetation, combining its spectral, textural, and phenological features from meter-level Gaofen images during 2019~2024. We found the optimal classification accuracy and processing time can be achieved with 2-m resolution imagery, with the overall classification accuracy of 92.4% and a Kappa coefficient of 0.89. Results of Tianjin Beidagang Wetland of Bohai Bay in North China indicate an increase in total carbon storage from 2.87 × 10^6 t C to 3.12 × 10^6 t C, with an average annual sequestration increase of 0.05 × 10^6 t C. Phragmites australis exhibited the highest carbon storage per unit area at 4.8 kg C/m^2/yr. The invasion of Spartina alterniflora enhanced local carbon storage by about 35%, potentially threatening the stability of the wetland carbon sink. This technical framework would be helpful for reducing the uncertainty of the coastal blue carbon assessment.

KEYWORDS
biomass inversion, carbon storage, coastal wetland, Gaofen satellite data, land cover classification

1 Introduction

Terrestrial plant photosynthesis absorbs carbon dioxide from the atmosphere. Research indicates that for every cubic meter of forest biomass growth, approximately 1.83 tons of CO_2 are captured from the atmosphere, while 1.62 tons of oxygen are released. The processes and mechanisms through which terrestrial vegetation captures, sequesters, and stores carbon are collectively termed the green carbon reservoir. Oceans cover 71% of the Earth's surface and host a vast array of microorganisms, seaweeds, seagrasses, and marine fauna, which possess carbon capture and storage functions analogous to terrestrial plants. In contrast to terrestrial green carbon, the process by which the ocean absorbs CO_2 from the atmosphere and fixes it is referred to as the marine or blue carbon reservoir. The concept of Blue Carbon was formally introduced in the 2009 report Blue

Carbon: The Role of Healthy Oceans in Binding Carbon jointly published by United Nations Environment Programme (UNEP) and others, primarily encompassing carbon storage in coastal wetlands such as mangroves, seagrass beds, and tidal marshes (Nellemann et al., 2009).

Coastal blue carbon ecosystems are characterized by high carbon storage capacity, rapid sequestration rates, and long-term stability. Located at the land-sea interface, coastal wetlands, despite comprising only about 0.05% of terrestrial biomass, are estimated to store and cycle nearly 55% of the carbon captured globally. Per unit area, carbon stocks in mangroves and salt marshes can be 3–5 times those of tropical forests (McLeod et al., 2011). Seagrass beds account for approximately 11% of the organic carbon buried in marine sediments globally, with the organic carbon stored in global seagrass sediments roughly equaling the sum stored in mangrove and salt marsh sediments. The carbon sequestration rate per unit area in mangroves and salt marshes is about ten times that of tropical forests. Furthermore, with climate warming and sea-level rise, the carbon sequestration capacity of salt marshes may increase further. Sediments constitute a major component of the coastal wetland carbon pool. The unique tidal hydrology of these areas creates predominantly anaerobic conditions in the sediments, significantly slowing the decomposition rate of organic carbon. In some regions, sediments can store carbon for millennia, as observed in mangrove sediments in Belize, Caribbean, tidal salt marshes in New England, and seagrass (Posidonia oceanica) meadows in Port Lligat Bay, Spain. Additionally, the presence of abundant electron acceptors (e.g., sulfate) in coastal wetland sediments can suppress methanogenesis by favoring sulfate-reducing bacteria. This shift in the microbial metabolic pathway, combined with the physical protection of organic matter within the sediment matrix, contributes to the long-term storage of carbon and reduces the emission of potent greenhouse gases like methane (Han et al., 2024).

To classify the types of vegetation in wetland, Han et al. (2024) achieved high-precision classification (Overall Accuracy 95.35%) of the Beidagang Wetland using the GEE platform, multi-source remote sensing data, and the Random Forest algorithm, providing a reliable data foundation for dynamic vegetation monitoring and carbon storage assessment (Han et al., 2014). Their earlier work on remote sensing-based wetland classification and drought monitoring (Han et al., 2014) also offers valuable insights into understanding wetland eco-hydrological processes and their response to climate change (Kearney et al., 2021). The Tianjin Beidagang Wetland Nature Reserve, a typical coastal wetland in Bohai Bay, serves as a crucial stopover site along the East Asian–Australasian Flyway and plays a significant role in carbon storage. In recent years, due to urban development in the Binhai New Area, the wetland ecosystem faces multiple pressures, including reclamation, pollution, and invasive species. Accurately monitoring vegetation distribution and its carbon storage capacity is essential for regional ecological conservation and achieving Carbon Peak and Carbon Neutrality goals (Dual Carbon goals).

Significant progress has been made globally in high-precision vegetation classification, biomass inversion, and carbon storage accounting. In stratified biomass estimation, studies have leveraged multi-source remote sensing, such as fusing satellite red-edge bands with radar data (Schmidt et al., 2021; Howard et al., 2017) or integrating Unmanned Aerial Vehicle (UAV) hyperspectral and satellite imagery (Li et al., 2022), to develop type-specific inversion models. Similarly, in carbon storage monitoring, advancements include the fusion of Light Detection and Ranging (LiDAR) with multispectral data for Three-Dimensional (3D) dynamic assessment (Long et al., 2021) and the coupling of remote sensing with ecosystem models to simulate carbon dynamics under climate change scenarios (Han et al., 2022; Breiman, 2001). The integration of Chinese high-resolution satellites [e.g., Gaofen (GF) series] and *in-situ* measurements has further enhanced the spatiotemporal resolution and accuracy of carbon stock mapping in coastal wetlands (Wang et al., 2023; Zhang et al., 2024a). However, a primary limitation is the poor transferability of site- or species-specific models across different regions or vegetation types (Sun et al., 2024; Howard et al., 2017; Wang et al., 2023). Technically, the effective fusion of multi-source data (e.g., optical, LiDAR, radar) remains challenging due to issues of scale, registration, and differing signal mechanisms (Li et al., 2022; Howard et al., 2017; Long et al., 2021; Zhang et al., 2024a). Furthermore, most models are built on single or limited-time snapshots, failing to adequately capture long-term vegetation and carbon dynamics driven by phenology, disturbances, and environmental changes (Han et al., 2022; Breiman, 2001). Finally, a deeper integration of remote sensing with process-based models is needed to improve the mechanistic understanding and predictive capability of the inversion. Previous studies have successfully applied multi-temporal remote sensing and multi-feature fusion to wetland vegetation classification and carbon estimation (Du et al., 2020; Wang et al., 2021; Liu et al., 2023; Kristin et al., 2018; Saintilan et al., 2022; Yang et al., 2016b; Zhang et al., 2024b).

Challenges remain in the synergistic use of multi-source high-resolution satellite data, stratified vegetation modeling strategies, and the effective fusion of sub-meter spatial details with multi-temporal features. Insufficient spatial resolution is a key technical bottleneck limiting estimation accuracy in coastal wetland carbon storage studies. Low-resolution imagery (e.g., 30 m Landsat, 10 m Sentinel-2) suffers from significant mixed-pixel problems, where a single pixel contains multiple land cover types (e.g., Suaeda salsa and bare soil, Phragmites australis and water), leading to mixed spectral responses and difficulty in accurately distinguishing vegetation types and their biomass. This is particularly problematic in the structurally complex and fragmented coastal wetland environment, where low-resolution data cannot capture fine boundaries and internal heterogeneity, causing classification errors to propagate into biomass inversion and carbon storage estimation, resulting in systematic bias.

Addressing the key issue of insufficient biomass estimation accuracy in blue carbon accounting, we innovatively propose a synergistic inversion method integrating domestic GF-1, GF-2, and GF-6 satellite data. The research leverages the multi-temporal observation capability of GF-1 (panchromatic (PAN) for 2 m and multi-spectral (MSS) for 8 m), the sub-meter high-resolution texture features of GF-2 (0.8 m PAN/3.2 m MSS), and the multispectral properties of GF-6 (2 m PAN/8 m MSS). Through multi-source data synergy and a stratified modeling strategy, we aim to overcome the limitations of single-data-source approaches for biomass estimation of Tianjin Beidagang wetland by the Bohai Bay in North China.

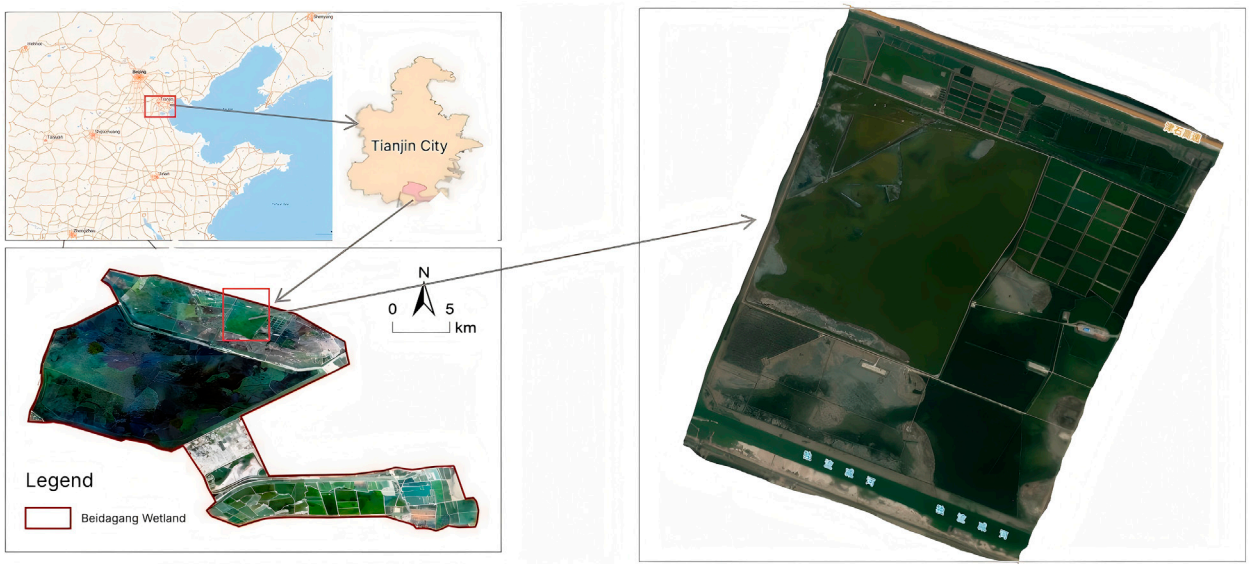


FIGURE 1
Tianjin beidagang wetland nature reserve by the bohai bay in north China.

TABLE 1 Satellite remote sensing data types and quantity statistics.

Data type	Date volume						
	2019	2020	2021	2022	2023	2024	Total
GF-2 (0.8 m)	2	1	1	2	2	1	9
GF-6 (2 m/8 m)	1	1	1	1	1	1	6
GF-1 (2 m/8 m)	1	1	1	1	1	1	6

2 Materials and methods

2.1 Study area

As shown in Figure 1, the Tianjin Beidagang Wetland Nature Reserve (38°46′–39°02′N, 117°18′–117°37′E) is located on the western coast of Bohai Bay, covering a total area of 348.87 km^2. It is characterized by a warm temperate semi-humid continental monsoon climate zone. The wetland features complete vegetation gradients, distinct disturbance gradients, good data availability, and urgent management needs. It holds significant representativeness and typicality for studying warm temperate coastal wetland ecosystems, serving as a natural laboratory for researching biodiversity maintenance, climate change response, and ecological processes under anthropogenic disturbance. Furthermore, as a key node on the East Asian–Australasian Flyway, the reserve possesses irreplaceable scientific value for bird ecology and migration studies.

2.2 Data source and preprocessing

Multi-temporal remote sensing data from 2019 to 2024 were acquired by the Chinese Gaofen series, including GF-1 (2 m/8 m), GF-2 (0.8 m/3.2 m), and GF-6 (2 m/8 m), as shown in Table 1. Image selection criteria required cloud cover of less than 5% and acquisition during key vegetation phenological periods (spring: April–May, summer: July–August, autumn: September–October), with the goal of obtaining at least one valid scene per season for each year. Owing to the challenge of frequent cloud cover in the Beijing-Tianjin-Hebei region, a rigorous screening process was applied. The final compilation of 21 qualified scenes (spring: 7, summer: 7, autumn: 7) thus forms a robust dataset suitable for long-term time-series analysis.

The main workflow consisted of: Radiometric calibration to convert digital numbers to top-of-atmosphere reflectance using ENvironment for Visualizing Images (ENVI) software. Atmospheric correction using the Fast Line-of-sight Atmospheric Analysis of Spectral Hypercubes (FLAASH) model to remove aerosol and water vapor effects. Geometric precision correction using 1: 10,000 topographic maps and Global Positioning System (GPS) ground control points, ensuring planar positional error within 0.5 pixels. Pan-sharpening of GF-2 and GF-6 data using the Gram-Schmidt method to generate 0.8 m and 2 m multi-spectral images, respectively; finally, image clipping based on the study area boundary vector. All data were unified to the WGS84 coordinate system and Universal Transverse Mercator (UTM) Zone 50N projection.

TABLE 2 Land cover classification standard.

Land cover type	NDVI range	NDWI range	GLCM contrast range	Key discriminating features
Tidal Flat	0 ~ 0.2	−0.2 ~ 0.2	5 ~ 15	Very low NDVI, weak NDWI, smooth texture
Herbaceous Marsh	0.4 ~0.7	0.3 ~ 0.6	35 ~ 70	Medium-high NDVI, high NDWI, cluttered texture (mixed withered grass)
Reservoir	<0.1	>0.6	0 ~ 5	Very low NDVI, very high NDWI, homogeneous texture (still water)
Bare Land	0 ~ 0.1	< −0.1	10 ~ 20	Very low NDVI, dry (very low NDWI), slightly rough
Buildings	0 ~ 0.1	< −0.1	50 ~ 150	Very low NDVI, very high contrast (regular geometric edges)
Spartina alterniflora	0.5 ~ 0.8	0.2 ~ 0.5	30 ~ 60	Moderately high NDVI, moderate NDWI, moderately rough texture
Phragmites australis	0.7 ~ 0.9	0.1 ~ 0.3	40 ~ 80	High NDVI, low NDWI, rough texture (stem shadows)
Suaeda salsa	0.2 ~ 0.5	−0.1 ~ 0.2	20 ~ 40	Low NDVI, saline soil distribution, patchy texture

2.3 Methods

2.3.1 Land cover classification based on multi-feature fusion

A three-dimensional classification system integrating Spectral-Moisture-Texture features was constructed. Using the Random Forest algorithm, we fused multi-temporal Normalized Difference Vegetation Index (NDVI), Normalized Difference Water Index (NDWI), and Gray-Level Co-occurrence Matrix (GLCM) texture features to classify eight land cover types: Water, Tidal Flat, Herbaceous Marsh, Phragmites australis, Suaeda salsa, Spartina alterniflora, Bare Land, and Buildings, as shown in Table 2. The thresholds for classification features were determined based on spectral data acquired from field sampling and high-resolution imagery in the study area, through quantitative statistics and separability analysis. This process was designed to provide feature inputs with clear physical meaning for subsequent machine learning classification.

Sample collection was based on GF-2 0.8-m high-resolution imagery. Initial manual annotation of typical land cover types in the core area was performed via visual interpretation in ENVI, supported by field survey photos (4 campaigns, 2022-2023) and Google Earth historical imagery. An improved the Support Vector Machine (SVM) active learning method was employed for intelligent sample expansion, utilizing dynamic spectral thresholds (±2σ) and spatial constraints (Wang and Xie, 2022), effectively avoiding cross-category contamination. During each active learning iteration, the Support Vector Machine (SVM) classifier was implemented with a Radial Basis Function (RBF) kernel, whose parameters were optimized via grid search combined with 5-fold cross-validation. After each iteration, the newly selected samples were incorporated into the existing training set to retrain the classifier, and its performance was evaluated on a fixed independent validation set consisting of 300 samples. In addition, we recorded the proportion of candidate samples ultimately selected in each iteration, as well as the distributional shifts of these samples in the feature space, thereby ensuring a progressive improvement in the diversity of the training dataset. Furthermore, a human-machine collaborative verification mechanism was implemented. First, confusion matrices were used to identify disputed samples. These samples were then arbitrated by experts, and finally, all samples were evaluated against a quality standard requiring a Kappa coefficient greater than 0.85 (Foody, 2020). This method reportedly increased sample generation efficiency threefold and improved overall classification accuracy by 12.6% ($p < 0.05$), with particularly notable improvement (18.3%) for easily confused classes like Suaeda salsa and Spartina alterniflora. The classification results are validated by the field investigation.

To ensure the adequacy of training samples, this study adopted a three-stage workflow comprising initial seed labeling, active learning-based iterative augmentation, and human-machine collaborative validation and adjudication. The execution conditions for each stage are as follows:

1. Initial seed sample generation: In the absence of any pre-existing sample library, spectrally and texturally pure areas with typical land cover characteristics were selected via visual interpretation based on 0.8 m GF-2 imagery. An initial seed set containing no fewer than 50 samples per class was constructed for eight land cover categories.
2. Active learning-based sample augmentation: This stage was initiated when the initial seed set had been established and preliminary classification results exhibited notable class confusion (e.g., misclassification rate between Suaeda salsa and Spartina alterniflora exceeding 20% in the confusion matrix). An improved SVM active learning strategy, incorporating boundary sampling and class-specific uncertainty weighting—systematically evaluated and adopted by Demir et al. (2012) for interactive classification of remote sensing imagery—was employed. In each iteration, 150–200 candidate pixels with the lowest classification confidence were selected and manually identified and labeled with reference to high-resolution image context. The termination criteria for this stage were as follows: (a) sample size per class reached 180–220; (b) improvement in overall classification accuracy between two consecutive iterations was less than 1.5%; (c) proportion of clearly identifiable new samples among the candidate pool fell below 30% upon manual inspection.
3. Human-machine collaborative validation and adjudication: Upon completion of the active learning stage, all accumulated

samples were systematically verified. High-uncertainty samples were first identified using out-of-bag (OOB) error estimates and cross-validation from the Random Forest classifier, followed by the screening of potential anomalous samples based on spectral thresholding (±2σ rule). These "disputed samples" were independently interpreted by two analysts; in cases of disagreement, a third expert made the final adjudication. This stage proceeded iteratively until the cross-validated Kappa coefficient of the entire sample set exceeded 0.85, and both producer's accuracy and user's accuracy for each land cover class surpassed 80%.

To scientifically evaluate the impact of spatial resolution on fine-scale coastal wetland classification and identify the optimal configuration, we designed a multi-resolution comparative experiment. The procedure was as follows: Using preprocessed and co-registered GF-2 imagery (0.8 m pansharpened multispectral data) as the baseline, an image pyramid with spatial resolutions of 0.8 m, 2 m, 5 m, and 10 m was generated via bilinear resampling. The following variables were controlled across all resolutions: identical training sample set (1,240 samples), identical feature set (spectral, textural, and phenological features), and identical Random Forest classifier parameters. Evaluation metrics included not only overall accuracy (OA) and Kappa coefficient, but also: (a) class-specific accuracy, particularly the user's and producer's accuracies for spectrally similar classes (Suaeda salsa, Spartina alterniflora, and herbaceous marsh); (b) classification uncertainty, quantified by the standard deviation of class probabilities derived from the Random Forest; (c) computational efficiency, recorded as the end-to-end processing time from feature extraction to classification completion; (d) landscape pattern indices, specifically differences in the number of patches (NP) and edge density (ED) derived from classification results at each resolution, to assess the impact of resolution on the representational capacity of landscape fragmentation. This experiment was designed to reveal, in a multi-dimensional manner, the trade-offs among accuracy, efficiency, and landscape representational capacity under varying spatial resolutions.

2.3.2 Stratified biomass inversion model

Above ground Biomass (AGB) is a key indicator for assessing vegetation productivity, carbon storage, and ecosystem health. Regression models between AGB and remote sensing-derived vegetation indices enable large-scale, efficient biomass estimation and are thus widely employed in wetland monitoring.

However, the relationship between spectral reflectance and AGB is strongly modulated by species-specific physiological structures, canopy geometries, and local environmental factors such as salinity and hydrological regime. These differences lead to substantial variability in the biomass–spectral response relationship across vegetation types (Ustin and Gamon, 2010). As noted by Homolová et al. (2013), developing a universal retrieval model applicable across diverse species and ecosystems remains a major challenge, particularly in species-rich and highly heterogeneous coastal wetlands. Applying a single generalized regression model under such conditions inevitably introduces systematic bias.

To address this issue, the present study adopts a species-specific stratified modeling strategy. For each dominant vegetation type, we independently selected the most appropriate published regression equation that: (i) has been validated in its native ecosystem, (ii) employs vegetation indices compatible with our satellite data (e.g., NDVI, SAVI, WDVI), and (iii) exhibits a functional form consistent with the target species' growth morphology and spectral characteristics. Although these equations originate from different geographic regions (e.g., the Yangtze Estuary, Yancheng coastal zone, Guangxi mangrove reserves), we assume that the biomass–reflectance relationship for the same species is transferable across similar wetland habitat types. Furthermore, all adopted models were locally calibrated and validated using field measurements collected in our study area (see Section 3.2), ensuring their applicability and accuracy in the Beidagang Wetland context. Table 3 presents the specific regression models developed between AGB and selected vegetation indices (WDVI, SAVI, and NDVI) for four typical wetland vegetation species.

Biomass retrieval for each vegetation type was conducted using the hierarchical models specified in Table 3. To ensure the applicability of these models—originally developed in disparate ecosystems—to the study area, we performed calibration or validation using field quadrat data collected from 2019 to 2023 (30 plots for Phragmites australis, 25 for Suaeda, 35 for Spartina alterniflora, and 20 for herbaceous marsh). As outlined in Table 3, local parameter calibration was applied to the Phragmites australis and herbaceous marsh models, whereas direct validation was adopted for the Suaeda and Spartina alterniflora models. The coefficients of determination (R^2) for model validation in the study area ranged from 0.78 to 0.89 (see Table 3 notes), demonstrating that—despite their diverse origins—the models, after targeted evaluation and necessary local adjustments, can robustly characterize the spatiotemporal biomass patterns of the major vegetation types in the Beidagang Wetland.

2.3.3 Carbon storage accounting method

Following the literature and the Intergovernmental Panel on Climate Change(IPCC) Wetlands Supplement guidelines, we integrated 6 years of vegetation classification and biomass data to construct a spatiotemporal carbon storage change model for the Beidagang Wetland, the standard carbon accounting formula is shown in Equation 1, where the total carbon storage is calculated as the product of the Above ground Biomass (AGB, t DM ha^{-1}), a carbon content coefficient, and the area (ha) of each vegetation class.

To evaluate the reliability of the estimated carbon storage values, independent validation was performed using 35 field plots surveyed in September 2023, none of which were involved in model training. The agreement between predicted and field-observed carbon storage was assessed using the mean absolute percentage error (MAPE) and a paired t-test, with results presented in Section 3.3.

$$Carbon\,Storage = AGB \times Carbon\,Content\,Coefficient \times Area \quad (1)$$

The corresponding carbon content coefficients for AGB from four land cover types were applied in Table 4.

TABLE 3 AGB regression models for different vegetation types.

Vegetation type	Vegetation indices	Regression model	References
Phragmites australis	WDVI	y = 181.72e5.0616x	Tian et al. (2016)
Suaeda salsa	SAVI	$y = -3.15 + 27.5x - 40.5x^2$	Wu et al. (2010)
Spartina alterniflora	NDVI	$y = 90.572x^2 - 213.303x + 1233.269$	Yang et al. (2023)
Herbaceous Marsh	NDVI	$y = 1250x^2 - 680x + 320$	Guangxi Mangrove Research Center (2019)

TABLE 4 AGB carbon content coefficients for different vegetation types.

Vegetation type	AGB carbon content coefficient (kg C/kg dry matter)	Key literature source
Phragmites australis	0.43	Brix et al. (2001)
Herbaceous Marsh	0.42	IPCC (2014)
Spartina alterniflora	0.47	Yang et al. (2016a)
Suaeda salsa	0.40	Zhou et al. (2020)

2.3.4 Controlled experiment on the effect of spatial resolution on classification accuracy

To quantitatively assess the impact of spatial resolution on fine-scale vegetation classification in coastal wetlands, we designed a controlled comparative experiment. The experiment utilized preprocessed GF-2 high-resolution imagery (0.8 m pan-sharpened multispectral) as the benchmark data source. Using resampling methods, the reference imagery was downscaled to spatial resolutions of 2 m, 5 m, 10 m, thereby generating a homologous experimental dataset with varying resolutions.

The core principle of the experiment was to maintain consistency across all other factors, modifying only the spatial resolution variable. The specific workflow was as follows:

1. Fixed sample set: Throughout the experiment, a unified set of training and validation samples, established based on high-resolution imagery and field surveys, was employed to ensure that classifiers at different resolutions utilized identical prior knowledge.
2. Unified feature extraction: For each resolution imagery, an identical set of remote sensing features was extracted, including spectral indices (e.g., NDVI, NDWI) and textural features. The calculation of textural features involved adjusting the window size in pixels according to the resolution to maintain consistent spatial representation.
3. Consistent classification workflow: All resolution images were classified using the same classification algorithm (Random Forest) and parameter settings, ensuring that any performance differences arose solely from changes in resolution.
4. Objective accuracy assessment: Using the same independent validation sample set, the overall accuracy, Kappa coefficient, and classification accuracy of major land-cover types were systematically evaluated and compared across different resolutions, while processing time was recorded to comprehensively assess efficiency.

This experimental design enabled the direct isolation and quantification of the effects of spatial resolution on final classification accuracy and efficiency, providing an objective basis for selecting 2 m as the optimal resolution in this study.

3 Results and analysis

3.1 Land cover classification: Accuracy assessment

To validate the effectiveness of multi-source data and feature fusion, we conducted controlled experiments using a September 2023 scene, as shown in Table 5. Compared to the baseline model using only spectral features, introducing phenological features increased Overall Accuracy (OA) by 3.6% and Kappa by 0.06; introducing high-resolution texture features yielded greater improvement (increasing OA by 6.4%). The final fused model used in this study, integrating all feature advantages, achieved an OA of 92.4%. Furthermore, User's Accuracy (UA) for easily confused classes improved markedly over the baseline: Spartina alterniflora by 20.1%, Phragmites australis by 10.7%, and herbaceous marsh by 13.6%. These results demonstrate the superiority of the multi-feature fusion strategy in resolving the classic remote sensing challenges of "same object with different spectra" and "different objects with the same spectrum" in coastal wetlands.

We tested the impact of different spatial resolutions on classification accuracy (Table 6). When resolution increased from 10 m to 2 m, OA increased by 12.9%, confirming the critical importance of high resolution for accuracy. Further improvement to 0.8 m yielded the highest accuracy but with diminishing returns and a substantial increase in computational cost. Thus, the 2 m resolution chosen in this study represents the optimal balance between high accuracy and efficiency. The mean annual Overall Accuracy for Random Forest classification from 2019 to 2024 was 92.4% ± 4.25%, with a mean Kappa coefficient of 0.89 ± 0.07. Classification accuracy for reservoir and Tidal Flat was stable

TABLE 5 Ablation study on feature contribution to classification accuracy (2023 September scene example).

Model description	Overall accuracy (OA)	Kappa coefficient	Alterniflora UA	*Phragmites australis* UA	Herbaceous marsh UA	S. Salsa UA
Spectral features only (GF-1/6)	82.5%	0.75	65.2%	80.1%	75.5%	70.3%
Spectral + Phenological features	86.1%	0.81	72.8%	84.5%	80.2%	75.6%
Spectral + Texture features	88.9%	0.85	78.5%	87.2%	84.8%	82.1%
This Study: Spectral + Texture + Phenology (Fused)	92.4%	0.89	85.3%	90.8%	89.1%	88.7%

TABLE 6 Impact of spatial resolution on classification performance.

Spatial resolution	Overall accuracy (OA)	Kappa coefficient	Relative computation time	Remarks
0.8 m	93.5%	0.91	~25 h	Contains significant detail noise, high computational load, low efficiency
2m	**92.4%**	**0.89**	**~2 h**	**Optimal balance of detail and computational efficiency (Selected)**
5 m	88.1%	0.83	~15 min	Mixed pixel issues begin to appear
10 m	79.5%	0.72	~2 min	Severe mixed pixel issues, vegetation

(Producer's Accuracy (PA) > 95%), while, in contrast, vegetation types showed greater variability, particularly in autumn.

The final sample set used in this study consisted of 1,320 samples, covering all eight land cover categories. Starting from an initial seed set of 400 samples, approximately 920 samples were augmented through three rounds of active learning iteration. Subsequently, approximately 7.5% of disputed samples were removed or corrected during the human-machine collaborative validation stage. Validation results demonstrated that the sample set obtained through this workflow supported an overall classification accuracy of 92.4% on the independent validation set, representing an improvement of approximately 8.2% compared to the classification result obtained using only the initial seed samples. Notably, the user accuracies for spectrally similar classes—such as Suaeda salsa and Spartina alterniflora—improved from 76.4% to 74.8%–88.7% and 85.3%, respectively. This confirms that the proposed sample workflow effectively mitigated spectral confusion between these confusable categories.

3.2 Spatiotemporal dynamics of land cover

Analysis of seasonal dynamics revealed a typical single-peak seasonal pattern in wetland vegetation cover (Figure 2). In spring (March–May), vegetation germination results in relatively low coverage. Rapid growth occurs in summer (May–September), with emergent plants such as Phragmites australis expanding considerably. Peak biomass is attained in autumn (September–November), though some vegetation senesces early due to harvesting or drought. Coverage decreases markedly in winter (December–February), accompanied by the expansion of tidal flats and bare ground. Water area dynamics are closely linked to precipitation, evaporation, and artificial regulation. Water area is relatively large in spring, contracts during summer due to high evaporation and vegetation water uptake, and partially recovers in autumn. In winter, the water area is substantially reduced as shallow waters freeze, leaving deep channels and artificial waterways as the primary water bodies.

Vegetation community succession exhibited clear trends. The dominant species, Phragmites australis, is primarily distributed along shallow water edges, has the longest growing season, and contributes the most biomass. Suaeda salsa becomes dominant in upland areas in autumn, but its distribution is constrained by salinity and moisture. Since its invasion in 2020, Spartina alterniflora has progressed from scattered patches to dominant communities in the southern and central areas. Its coverage increased by 18% from 2019 to 2023, demonstrating significantly enhanced ecological competitiveness. Landscape pattern changes from 2019 to 2024 showed an alternating expansion-contraction pattern for water and vegetation. Ecological connectivity was higher in spring and summer, favoring waterbird habitat, while fragmentation increased significantly in winter, limiting overwintering species. Compounding these seasonal dynamics, the invasion of Spartina alterniflora further intensified spatial heterogeneity and competitive pressure within the ecosystem.

The Sankey diagram shown in Figure 3 was generated based on land-use transfer matrices derived from the classification results of the 2019 and 2024 time periods. To enhance readability and effectively convey key information, this visualization tool applies a default flow filtering threshold, displaying only those transitions accounting for more than 1% of the total converted area. During the 2019–2024 period, the core driving force of landscape change was the large-scale expansion of Spartina alterniflora and its replacement

10.3389/frsen.2026.1742193

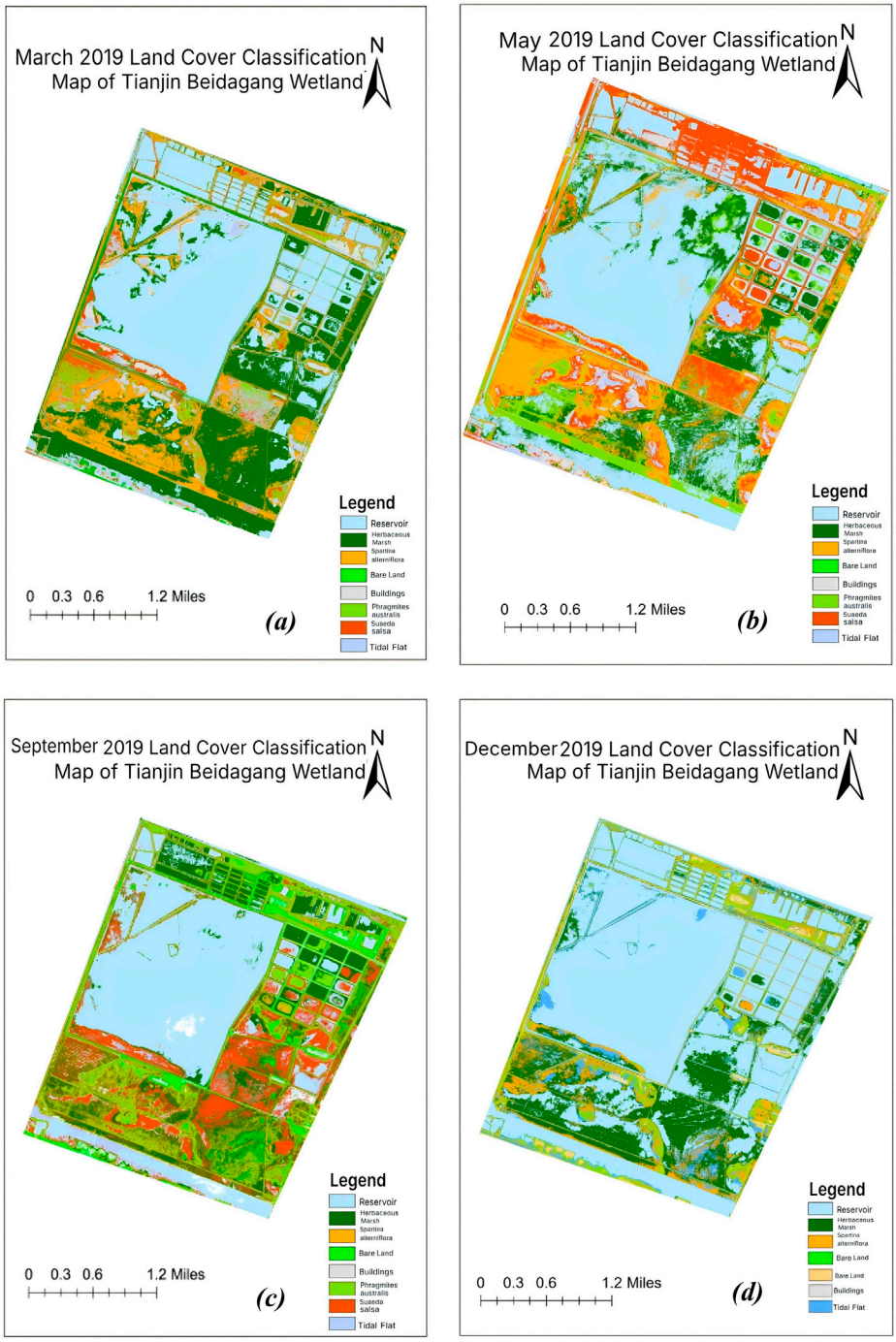


FIGURE 2
(a) Land cover classification map of the Tianjin Beidagang Wetland in March 2019, showing the distribution of key vegetation types and land cover features at the beginning of the growing season. **(b)** Land cover classification map of the Tianjin Beidagang Wetland in May 2019, depicting mid-spring conditions with advancing plant growth and changes in wetland coverage. **(c)** Land cover classification map of the Tianjin Beidagang Wetland in September 2019, capturing peak biomass period and mature vegetation distributions before autumn senescence. **(d)** Land cover classification map of the Tianjin Beidagang Wetland in December 2019, showing winter conditions with dormant vegetation and exposed land surfaces.

of Suaeda and tidal flats—transitions that constituted the predominant, macroscopically visible "wide flows." In contrast, Phragmites australis communities exhibited relatively stable distribution over this period, with conversions involving Phragmites australis (either to or from other types) all falling below the 1% threshold. Similarly, although remnant patches of Suaeda persisted in 2024, most mutual conversions between Suaeda and other land-cover types remained below the threshold. Consequently, they are not displayed as prominent inflow or outflow nodes in the 2024 segment of the diagram.

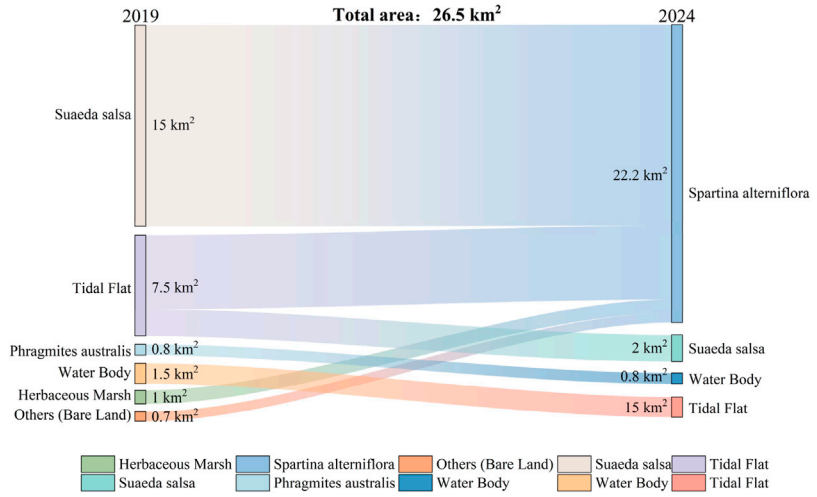


FIGURE 3
Sankey diagram of area conversion pathways for major land classes in beidagang wetland (2019–2024).

Based on the land use transition matrix derived from overlaid classification results, this Sankey diagram visually reveals the area conversion pathways and fluxes of core land classes during the study period. Flow width is proportional to the conversion area. The results indicate that the invasion of Spartina alterniflora was the dominant driver of wetland landscape pattern change. Its areal expansion primarily resulted from the replacement of Suaeda salsa and Tidal Flats, with conversion areas as high as 15.0 km^2 and 5.5 km^2, respectively, forming the widest flows in the diagram. This demonstrates the strong competitive and replacement ability of Spartina alterniflora in the intertidal zone. Minor conversion pathways included the transformation of Tidal Flat to Suaeda salsa (2.0 km^2), reflecting natural succession or salinity changes in terrestrial fringe areas; siltation of water to Tidal Flat (1.5 km^2), indicating natural sediment deposition; and sporadic conversion of Phragmites australis to water (0.8 km^2), potentially related to localized water level rise or flooding stress. Overall, the Sankey diagram depicts the evolution pattern of the Beidagang Wetland landscape: the native Suaeda salsa and natural Tidal Flat ecosystems are being extensively replaced by the invasive Spartina alterniflora, constituting the most significant landscape dynamic during the study period.

Figure 4 presents the interannual variations in area derived from the optimal classification results obtained during the peak growing season (autumn) of each year. This approach effectively filters out seasonal noise, thereby clearly revealing the dominant long-term ecological process of Spartina alterniflora invasion and the concurrent decline of native Suaeda salsa. The left axis of Figure 4 highlights a critical ecological shift, where native Suaeda salsa declined by 18.0 km^2 while invasive Spartina alterniflora expanded by the same amount, suggesting competitive displacement. The right axis of Figure 4 provides context by showing that water bodies and tidal flats remained largely stable, with only a minor decline in Phragmites australis.

Figure 4 shows that the interannual area dynamics of major land classes in the Beidagang Wetland from 2019 to 2024 quantitatively reveal a dramatic ecological shift dominated by invasive species.

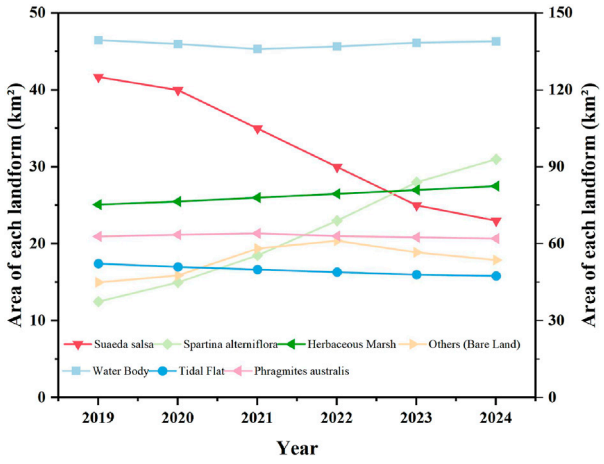


FIGURE 4
Interannual dynamics (2019–2024) of major land class areas in beidagang wetland.

Over the 6 years, the landscape structure underwent fundamental reorganization, characterized most notably by the explosive expansion of Spartina alterniflora and the catastrophic decline of native Suaeda salsa communities. Specifically, the area of Spartina alterniflora increased continuously from 12.5 km^2 in 2019 to 31.0 km^2 in 2024, a net increase of 18.5 km^2 (148% expansion, >24% annual rate). Its proportional coverage rose from 3.6% to 8.9%, transforming it from a minor component to a dominant landscape element. In stark contrast, the area of Suaeda salsa plummeted from 41.7 km^2 in 2019 to 23.0 km^2 in 2024, a net loss of 18.7 km^2 (45% decline). Notably, the loss of Suaeda salsa (18.7 km^2) closely matches the gain in Spartina alterniflora (18.5 km^2). Combined with the Sankey diagram, Figure 3 indicates that Spartina alterniflora invasion is the primary driver of Suaeda salsa recession, with its expansion directly replacing

Suaeda salsa habitat. Water bodies and Phragmites australis remained highly stable during this period, with interannual fluctuations less than 3.5 km^2 and 2.0 km^2, respectively, suggesting the fundamental hydrological environment and Phragmites australis-dominated community structure remained largely intact. Herbaceous marsh area increased slowly by ~2.4 km^2, possibly linked to localized hydrological changes. Tidal Flat area decreased by 4.8 km^2, partly converted to Spartina alterniflora and Suaeda salsa. Other types showed minor fluctuations, having little impact on the overall pattern.

3.3 Biomass inversion

Leveraging multi-temporal remote sensing inversion data from 2019 to 2024, we systematically analyzed the spatiotemporal changes and driving mechanisms of AGB for four major vegetation types in the Beidagang Wetland. Results indicate: Temporal Dynamics: AGB showed a significant seasonal single-peak pattern, peaking in September (>2.0 kg/m^2) and reaching lows in March–April (0.3–0.6 kg/m^2). Spatial Pattern: High AGB areas expanded from the shoreline towards the wetland center, controlled by the water level gradient. Specifically, high spring water levels restricted high biomass to near-shore areas; receding levels in summer and autumn enabled its expansion toward the center; and winter contraction caused these areas to recede to the southwest, which became dominated by Spartina alterniflora. Species Differences: Phragmites australis AGB showed significant seasonal fluctuation but relative interannual stability, with a recovery trend in 2024. Suaeda salsa AGB exhibited high interannual variability, significantly correlated with tidal inundation frequency. Spartina alterniflora AGB was stable, with high winter values concentrated in the southwest, reflecting its strong cold tolerance and possible management. Herbaceous marsh AGB stabilized after 2020, showing a growth trend in 2023–2024, potentially linked to vegetation restoration projects.

The boxplot components represent the distribution of AGB for each vegetation type across the six sampling years: the box spans the interquartile range (IQR, 25th–75th percentiles), the horizontal line inside the box denotes the median, and the whiskers extend to the minimum and maximum values within 1.5 × IQR. Values beyond the whiskers are plotted as individual points, indicating potential outliers. The overlaid scatter plot displays the annual AGB measurements for each vegetation type. Each symbol corresponds to a specific year (2019–2024), and its position on the y-axis (AGB, g/m^2) represents the biomass value recorded in that year (as detailed in Table 3). This combined visualization allows simultaneous assessment of interannual variability and overall distributional characteristics across vegetation types.

Boxplot analysis of AGB for major vegetation species from 2019 to 2024 revealed distinct differences in growth dynamics, as shown in Figure 5. Biomass stability ranked: Spartina alterniflora > Phragmites australis ≈ Herbaceous Marsh > Suaeda salsa, reflecting different environmental adaptation strategies. Spartina alterniflora AGB exhibited exceptionally high interannual stability, with the median consistently within the narrow range of 1150 - 1200 g/m^2 and compact boxes indicating minimal fluctuation. This suggests the invasive species has established a robust niche in the Beidagang environment, largely unaffected by interannual climate variation, supporting its continued expansion. In contrast, Suaeda salsa AGB showed dramatic interannual fluctuations. Its boxes were generally longer, and a significant low median value occurred in 2021. Phragmites australis, as the dominant species, maintained relatively high and stable AGB levels (median range ~280 - 450 g/m^2), consistent with its stable dominant status. Herbaceous marsh biomass showed moderate fluctuation, with an outlier high value observed in autumn 2020 (886.81 g/m^2), possibly related to particularly favorable hydrothermal conditions that year. In summary, Beidagang Wetland AGB dynamics are driven by the coupled effects of hydrological rhythm, climate fluctuation, species adaptability, and human intervention, which exhibits characteristics of seasonal expansion - interannual fluctuation - species differentiation.

3.4 Carbon storage estimation and its implications for carbon sink stability

Interannual Trend in Figure 6: Total carbon storage increased from 2.87×10^6 t C in 2019 to 3.12×10^6 t C in 2024, with an average annual sequestration increase of 0.05×10^6 t C, equivalent to absorbing approximately 1.8% of Tianjin's annual carbon emissions. Phragmites australis had the highest carbon storage per unit area (4.8 kg $C/m^2/yr$), compared to 1.8 kg $C/m^2/yr$ for Suaeda salsa. Spartina alterniflora invasion increased local carbon storage by 35%, but its ecological competitiveness may threaten the long-term stability of the wetland carbon sink.

Based on the AGB inversion results and species-specific carbon content coefficients, we estimated the total carbon storage of the Beidagang Wetland from 2019 to 2024. The total carbon storage increased from 2.87×10^6 t C in 2019 to 3.12×10^6 t C in 2024, with an average annual sequestration of 0.05×10^6 t C. Seasonal dynamics closely followed vegetation phenology, peaking in September and reaching a nadir in March–April.

Significant interspecific differences were observed in carbon storage per unit area. Phragmites australis exhibited the highest carbon density (4.8 kg $C/m^2/yr$), followed by Spartina alterniflora (3.2 kg $C/m^2/yr$) and herbaceous marsh (2.5 kg $C/m^2/yr$), whereas Suaeda salsa showed the lowest value (1.8 kg $C/m^2/yr$). Spatially, carbon storage hotspots were concentrated in the southwestern region, where S. alterniflora has formed extensive continuous stands, corroborating the high productivity of this invasive species.

4 Conclusion and discussion

This study, based on multi-source remote sensing data (2019–2024) from the domestic Gaofen satellite series (GF-1/2/6) and the fusion of spectral, textural, and phenological features, systematically revealed the spatiotemporal dynamics of carbon storage in the Tianjin Beidagang Wetland. The constructed Random Forest classification model achieved an overall accuracy of 92.4% (Kappa coefficient 0.89) for eight land cover types including Phragmites australis, Suaeda salsa, Spartina alterniflora, and herbaceous marsh. The user accuracies for Spartina alterniflora, Phragmites australis, herbaceous marsh, and Suaeda salsa reached 85.3%, 90.8%, 89.1%, and 88.7%, respectively.

A key methodological contribution of this work lies in its explicit targeting of small-scale wetland patches—an ecologically critical yet persistently under-mapped category in existing land cover datasets.

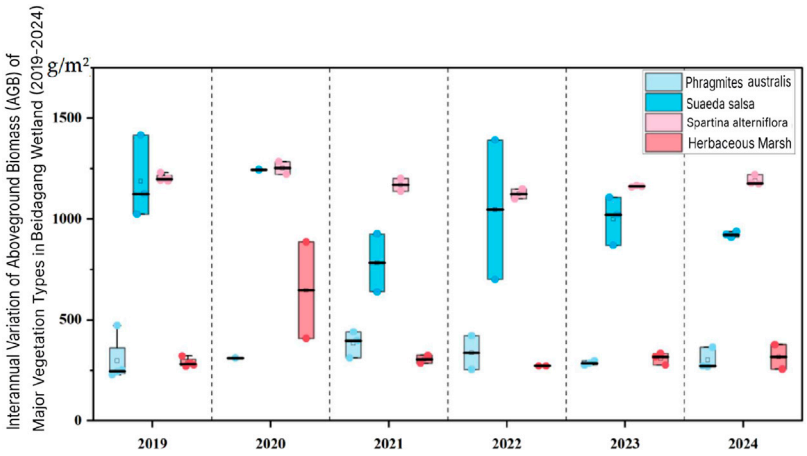


FIGURE 5
Boxplots and scatter plots depicting the Above ground Biomass (AGB, g/m^2) of four vegetation types (Phragmites australis, Suaeda salsa, Spartina alterniflora, and herbaceous marsh) over the period 2019–2024.

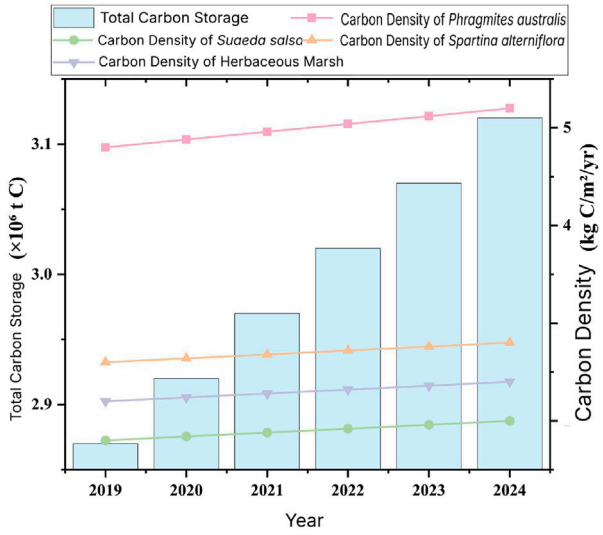


FIGURE 6
Carbon storage and its interannual variation in beidagang wetland (2019-2024).

Widely used products such as GWL_FCS30 and 10 m/30 m Sentinel-2/Landsat maps are optimized for continental consistency, but their spatial resolution inherently omits water bodies and vegetation patches smaller than 0.1 ha, leading to substantial underestimation of wetland extent and habitat fragmentation in coastal landscapes. Conversely, sub-meter imagery (0.8 m) provides sufficient detail but is constrained by prohibitive acquisition costs and limited swath, rendering it impractical for routine regional monitoring. The visibility of Phragmites australis varies with spatial resolution due to the mixed pixel effect, where coarser resolutions integrate sparse vegetation and bare soil into a single class. To ensure the robustness of our temporal trends, we maintained consistent resolution and classification methods across all years. Our spatial resolution comparison indicates that 2-m resolution strikes an optimal balance between mapping granularity and operational feasibility, and is recommended as a cost-effective "sweet spot" for prefecture-to provincial-scale coastal wetland assessments. This finding advocates a resolution-aware, region-specific strategy rather than a one-size-fits-all paradigm—a perspective that is often overlooked in current large-scale mapping efforts.

Landscape pattern analysis revealed a fundamental ecosystem reorganization, dominated by the invasion of Spartina alterniflora. The invader's area surged from 12.5 km^2 to 31.0 km^2, primarily through the direct replacement of native Suaeda salsa habitat, which consequently plummeted from 41.7 km^2 to 23.0 km^2. Biomass analysis indicated a significant single-peak seasonal variation in Above ground Biomass, peaking in September, with interannual stability across vegetation types ranking as Spartina alterniflora > Phragmites australis ≈ Herbaceous Marsh > Suaeda salsa. The median biomass of Spartina alterniflora remained stable at 1150–1200 g/m^2, herbaceous marsh and Phragmites australis showed comparable stability, while Suaeda salsa exhibited strong fluctuations.

Carbon storage accounting results showed that the total wetland carbon storage increased from 2.87×10^6 t C in 2019 to 3.12×10^6 t C in 2024, with an average annual sequestration of 0.05×10^6 t C; its seasonal dynamics closely followed vegetation phenology. Phragmites australis demonstrated the highest carbon storage per unit area (4.8 kg C/m^2/yr), significantly exceeding Suaeda salsa (1.8 kg C/m^2/yr). Despite increasing local carbon storage by 35%, the invasion of Spartina alterniflora poses a potential threat to the long-term stability of the wetland carbon sink due to its strong ecological competitiveness.

We therefore position our approach not as a competitor to global wetland products, but as a high-resolution complement that fills the critical "small wetland blind spot" —serving as a calibration reference, validation tier, or downscaling basis for coarser datasets. This niche is both technically underexplored and practically urgent for local wetland conservation and restoration planning. Future work will extend this meter-scale, small-wetland-aware framework to larger climatic and geographic zones across China, systematically evaluating its robustness and transferability under varied environmental conditions.

Data availability statement

The original contributions presented in the study are included in the article/supplementary material, further inquiries can be directed to the corresponding author.

Author contributions

YG: Data curation, Visualization, Investigation, Software, Resources, Writing – original draft, Validation. YW: Formal Analysis, Project administration, Conceptualization, Methodology, Writing – review and editing, Supervision, Funding acquisition, Resources. LZ: Formal Analysis, Validation, Data curation, Writing – review and editing, Methodology, Investigation, Resources, Visualization. WW: Project administration, Formal Analysis, Supervision, Funding acquisition, Writing – review and editing, Investigation. QC: Investigation, Validation, Software, Resources, Formal Analysis, Data curation, Writing – original draft. XH: Project administration, Validation, Resources, Methodology, Writing – review and editing, Data curation, Conceptualization. CX: Methodology, Project administration, Funding acquisition, Supervision, Formal Analysis, Software, Writing – review and editing. PL: Methodology, Data curation, Investigation, Visualization, Validation, Writing – review and editing, Project administration. XS: Formal Analysis, Writing – original draft, Validation, Software, Conceptualization. XnZ: Software, Writing – original draft, Investigation, Data curation, Conceptualization. MJ: Investigation, Methodology, Writing – original draft, Validation, Resources, Visualization. ZL: Validation, Visualization, Writing – original draft, Data curation. YW: Writing – original draft, Validation, Investigation. XyZ: Writing – original draft, Resources, Investigation.

Funding

The author(s) declared that financial support was received for this work and/or its publication. This research was funded by National Key Research and Development Program of China, grant 2022YFB3902200; Tianjin Municipal Natural Science Foundation, grant 24JCZDJC01120; Beijing Engineering Research Center of Aerial Intelligent Remote Sensing Equipments Fund, grant AIRSE202408; the Fundamental Research Funds for the Central Universities and the Research Funds of Renmin University of China, grant 22XNLG03.

Acknowledgements

We appreciate the data provided by the Tianjin Bohai Rim Coastal Earth Critical Zone National Observation and Research Station for ground validations.

Conflict of interest

The author(s) declared that this work was conducted in the absence of any commercial or financial relationships that could be construed as a potential conflict of interest.

Generative AI statement

TThe author(s) declared that generative AI was not used in the creation of this manuscript.

Any alternative text (alt text) provided alongside figures in this article has been generated by Frontiers with the support of artificial intelligence and reasonable efforts have been made to ensure accuracy, including review by the authors wherever possible. If you identify any issues, please contact us

Publisher's note

All claims expressed in this article are solely those of the authors and do not necessarily represent those of their affiliated organizations, or those of the publisher, the editors and the reviewers. Any product that may be evaluated in this article, or claim that may be made by its manufacturer, is not guaranteed or endorsed by the publisher.

References

Breiman, L. (2001). Random forests. *Mach. Learn.* 45 (1), 5–32. doi:10.1023/a:1010933404324

Brix, H., Sorrell, B. K., and Lorenzen, B. (2001). Are phragmites-dominated wetlands a net source or net sink of greenhouse gases? *Aquat. Bot.* 69 (2-4), 313–324. doi:10.1016/s0304-3770(01)00145-0

Demir, B., Bovolo, F., and Bruzzone, L. (2012). Detection of land-cover transitions in multitemporal remote sensing images with active-learning-based compound classification. *IEEE Trans. Geoscience Remote Sens.* 50 (5), 1930–1941. doi:10.1109/tgrs.2011.2168534

Du, L., McCarty, G., Zhang, X., Lang, M., Vanderhoof, M., Li, X., et al. (2020). Phenology-based classification of coastal wetland vegetation using Landsat-8 time series. *Int. J. Appl. Earth Observation Geoinformation* 90, 102131. doi:10.1016/j.jag.2020.102131

Foody, G. M. (2020). Integrating expert knowledge in sample validation. *Remote Sens.* 12 (5), 823. doi:10.3390/rs12050823

Guangxi Mangrove Research Center. (2019). *Dataset of mangrove and coastal wetland biomass in Guangxi mangrove reserve (2015–2019)* Unpublished dataset

Han, X., Feng, L., Hu, C., and Chen, X. (2014). Wetland changes of China's largest freshwater lake and their linkage with the Three Gorges Dam. *Remote Sens. Environ.* 204, 799–811. [Chinese Journal. doi:10.1016/j.rse.2017.09.023

Han, Z., Li, Z., Sun, Y., and Liu, D. (2022). Construction and application of a remote sensing assessment model for carbon storage in the Yellow River Delta wetland. *Sci. China Earth Sci.* 52 (6), 1123–1136. [In Chinese]. doi:10.13203/j.whugis20200095

Han, Z., Jin, K., Zong, Q., Qin, P., Liu, C., and Zhu, X. (2024). *High-precision classification of Beidagang Wetland based on GEE platform and multi-source remote sensing data using Random Forest.* [Manuscript under review].

Homolová, L., Malenovský, Z., Clevers, J. G., García-Santos, G., and Schaepman, M. E. (2013). Review of optical-based remote sensing for plant trait mapping. *Ecol. Complex.* 15, 1–16. doi:10.1016/j.ecocom.2013.06.003

Howard, J., Sutton-Grier, A., Herr, D., Kleypas, J., Landis, E., Mcleod, E., et al. (2017). Coastal blue carbon: methods for assessing carbon stocks and emissions factors in mangroves, tidal salt marshes, and seagrass meadows. *Nat. Clim. Change* 7 (9), 673–677. doi:10.3389/fmars.2017.00192

IPCC (2014). "2013 supplement to the 2006 IPCC Guidelines for national greenhouse gas inventories: wetlands," *IPCC*

Kearney, M. S., Thomas, N., Turner, E., McCarty, J., Bostater, C., Hall, F., et al. (2021). Sentinel-2 remote sensing of Zostera noltei-dominated intertidal seagrass meadows. *Remote Sens. Environ.* 263, 112549. doi:10.1016/j.rse.2020.112020

Kristin, B. B., Ballanti, L., Nathan, M. T., Nguyen, D., James, R. H., Simard, M., et al. (2018). Evaluation of Sentinel-2 for mapping wetland vegetation biomass at multiple scales. *Remote Sens.* 10 (7), 1099. doi:10.1002/fee.1937

Long, X., Li, X., Lin, H., and Zhang, M. (2021). Coastal wetland vegetation classification method based on Sentinel-2 red-edge bands. *J. Remote Sens.* 25 (4), 892–905. [In Chinese].

Li, H., Wan, J., Liu, S., Sheng, H., and Xu, M. (2022). Phragmites australis biomass estimation in coastal wetlands based on synergy of GF-2 and GF-1 data. *Remote Sens. Technol. Appl.* 37 (2), 345–356. [In Chinese].

Liu, Z. (2023). Fine classification of coastal wetland vegetation using Sentinel-2 time-series red-edge features and deep learning. *ISPRS J. Photogrammetry Remote Sens.* 195, 1–15.

McLeod, E., Chmura, G. L., Bouillon, S., Salm, R., Björk, M., Duarte, C. M., et al. (2011). A blueprint for blue carbon: toward an improved understanding of the role of vegetated coastal habitats in sequestering CO2. *Front. Ecol. Environ.* 9 (10), 552–560. doi:10.1890/110004

Nellemann, C., Corcoran, E., Duarte, C. M., Valdes, L., and Young, C. D. (2009). Blue carbon: The role of healthy oceans in binding carbon. Arendal, Norway: GRID-Arendal.

Saintilan, N., et al. (2022). Climate-driven shifts in sediment dynamics enhance carbon accumulation in blue-carbon ecosystems. *Glob. Change Biol.* 28 (8), 2531–2545.

Schmidt, K. S., et al. (2021). Multi-scale fusion of UAV hyperspectral and Sentinel-2 multispectral data for improved biomass estimation in heterogeneous wetlands. *Sci. Total Environ.* 789, 147856. doi:10.3390/rs13132495

Sun, W., Chen, D., Li, Z., Li, S., Cheng, S., Niu, X., et al. (2024). A hierarchical biomass inversion model for coastal wetland vegetation by integrating GF-6 red-edge bands and Sentinel-1 radar data. *Ecol. Indic.* 158, 111325.

Tian, S., Zhang, X., Tian, J., and Sun, Q. (2016). Modeling the above ground Biomass of Phragmites australis in the Yangtze River Estuary using remote sensing and environmental data. *Acta Ecol. Sin.* 36 (19), 6132–6143. [In Chinese].

Ustin, S. L., and Gamon, J. A. (2010). Remote sensing of plant functional types. *New Phytol.* 186 (4), 795–816. doi:10.1111/j.1469-8137.2010.03284.x

Wang, X.-F., and Xie, P.-F. (2022). Dynamic threshold SVM for sample selection. *IEEE Trans. Geoscience Remote Sens.* 60, 1–15.

Wang, Z. (2021). Wetland vegetation classification in the Yellow River Delta using GF-6 red-edge bands. *J. Remote Sens.* 25 (4), 892–905. [In Chinese].

Wang, R., et al. (2023). A synergistic framework for high spatiotemporal resolution mapping of coastal blue carbon stocks by integrating multi-source Chinese high-resolution satellites and UAV LiDAR. *Remote Sens. Environ.* 289, 113512. doi:10.1016/j.rse.2023.113512

Wu, T., Zhao, D-Z., Kang, J., Suo, A-N., Wei, B-Q., Ma, Y-J., et al. (2010). Estimation of Suaeda salsa above ground Biomass in coastal wetlands based on hyperspectral remote sensing and SAVI. *Spectrosc. Spectr. Analysis* 30 (8), 2184–2188. [In Chinese].

Yang, W., Zhao, H., and Yue, L. (2016a). Carbon storage and sequestration of Spartina alterniflora salt marshes in the Yellow River Delta, China. *Estuar. Coast. Shelf Sci.* 180, 82–91. doi:10.1016/j.ecss.2016.07.012

Yang, W., Yan, Y., Jiang, F., Leng, X., Cheng, X., and An, S. (2016b). Response of the soil microbial community composition and biomass to a short-term Spartina alterniflora invasion in a coastal wetland of eastern China. *Plant Soil* 408 (1-2), 443–456. doi:10.1007/s11104-016-2941-y

Yang, Z., Huang, Y., Duan, Z., and Tang, J. (2023). Inversion of Above ground Biomass of Spartina alterniflora in Yancheng coastal wetland based on NDVI and machine learning. *Remote Sens. Technol. Appl.* 38 (4), 912–923. [In Chinese].

Zhang, L. (2024a). Impacts of Spartina alterniflora invasion on coastal blue carbon stocks: gains in initial invasion *versus* long-term stability risks. *Sci. Total Environ.* 907, 167932. doi:10.1016/j.scitotenv.2023.167932

Zhang, Z., Xia, X., Chen, L., Liang, H., Zhao, X., Liu, B., et al. (2024b). Geomorphological changes and sediment carbon accumulation at the bare mudflat-saltmarsh interface: the role of typhoons. *Geomorphology* 451, 109151. doi:10.1016/j.geomorph.2024.109151

Zhou, M. X., Li, X. Z., and Gao, Y. (2020). Carbon stock and sequestration potential of Suaeda salsa wetlands in the Liaohe Delta, China. *Ecol. Indic.* 113, 106–204. doi:10.1016/j.ecolind.2020.106204